Tailoring the structure and thermoelectric properties of $BaTiO_3$ via Eu^{2+} substitution

Xingxing Xiao [a], Marc Widenmeyer [a], Wenjie Xie [a], Tianhua Zou [a], Songhak Yoon [a], Marco Scavini [b,d], Stefano Checchia [b], Zhicheng Zhong[c], Philipp Hansmann[c], Stefan Kilper [a], Andrei Kovalevsky [e], Anke Weidenkaff [a]*

[a] University of Stuttgart, Institute for Materials Science, Heisenbergstr. 3, 70569 Stuttgart, Germany

[b] University of Milan, Chemistry Department, Via C. Golgi 19, I-20133 Milano, Italy,

[c] Max Planck Institute for Solid State Research, Heisenbergstr. 1, 70569 Stuttgart, Germany

[d] CNR-ISTM, Ist. Sci. & Tecnol. Mol., I-20133 Milan, Italy

[e] CICECO - Aveiro Institute of Materials, University of Aveiro, Department of Materials and Ceramic Engineering, 3810-193 Aveiro, Portugal

* Email: weidenkaff@imw.uni-stuttgart.de

Abstract:

A series of $Ba_{1-x}Eu_xTiO_{3-\delta}$ ($0.1 \leq x \leq 0.9$) phases with ~ 40 nm particle size were synthesized via a Pechini method followed by annealing and sintering under reducing atmosphere. The effects of Eu^{2+} substitution on the $BaTiO_3$ crystal structure and thermoelectric transport properties were systematically investigated. According to synchrotron X-ray diffraction data only cubic perovskite structures were observed. On the local scale below about 20 Å (equal to ~ 5 unit cells) deviations from the cubic structure model ($Pm\bar{3}m$) were detected by evaluation of the pair distribution function (PDF). These deviations cannot be explained by a simple symmetry breaking model like in $EuTiO_{3-\delta}$. The best fit was achieved in space group *Amm*2 allowing for a movement of Ti and Ba/Eu along <110> of the parent unit cell as observed for $BaTiO_3$. Density functional calculations delivered an insight into the electronic structure of $Ba_{1-x}Eu_xTiO_{3-\delta}$. From the obtained density of states a significant reduction of the band gap by the presence of filled Eu^{2+} 4*f* states at the top of the valence band was observed. The physical property measurements revealed that barium europium titanates exhibit n-type semiconducting behavior and that at high temperature the electrical conductivity is strongly depended on the Eu^{2+} content. Activation energies calculated from the electrical conductivity and Seebeck coefficient data indicate that at high temperature (800 K < *T* < 1123 K) the conduction mechanism of $Ba_{1-x}Eu_xTiO_{3-\delta}$ ($0.1 \leq x \leq 0.9$) is a polaron hopping when $0 < x \leq 0.6$ and is a thermally activated process when $0.6 < x < 1$.

Besides, the thermal conductivity increases with increasing Eu^{2+} concentration. Due to a remarkable improvement of the power factor, $Ba_{0.1}Eu_{0.9}TiO_{3-\delta}$ showed a *ZT* value of 0.24 at 1123 K.

Key words: perovskite, thermoelectric properties, XRD, PDF, europium

1. Introduction

$BaTiO_3$ is one of the most intensively investigated perovskite-type (ABO_3) oxide materials due to its rich physical properties such as ferroelectricity[1], piezoelectricity [2], high dielectric constant[3], etc.[4-6]. While $EuTiO_3$ is a well-known magnetic material especially renowned for its G-type antiferromagnetic (AFM) configuration below Néel temperature (T_N = 5.3 K)[7,8], it is a promising candidate as ferromagnetic and ferroelectric material[9]. The compounds $Ba_{1-x}Eu_xTiO_{3-\delta}$ can be regarded as a $BaTiO_3$–$EuTiO_3$ solid solution. Based on the combination of these inherent properties from original system $BaTiO_3$ (ferroelectric-nonmagnet)[10] and $EuTiO_3$ (paraelectric-antiferromagnet)[11], it is highly possible to give rise to some exceptional phenomena, such as multiferroicity, magnetocaloric effects, thermoelectricity, et cetera. For instance, $Eu_{0.5}Ba_{0.5}TiO_3$ exhibits simultaneously fairly large ferroelectricity and a magnetic moment[12]. It was confirmed to be a multiferroic material used to search for the permanent electric dipole moment of the electron[13]. The compounds of $Eu_{1-x}Ba_xTiO_{3-\delta}$ family exhibit giant magnetocaloric effect, indicating that these compounds could be potential candidates for cryogenic magnetic refrigeration[14]. Accordingly, $Ba_{1-x}Eu_xTiO_{3-\delta}$ is a very interesting multifunctional oxide ceramic material, which has been extensively studied for various applications[15,16]. However, to the best of our knowledge there are no systematic studies about the thermoelectric properties of this material, though it could be a potential candidate in thermoelectric application according to our theoretical predictions and its applicability.

The performance of thermoelectric materials is evaluated by a dimensionless figure of merit value which is defined by $ZT = (S^2\sigma T)/\kappa$, where S is the Seebeck coefficient, σ the electrical conductivity, κ the thermal conductivity and T the absolute temperature. A good thermoelectric material should have a high Seebeck coefficient S, good electric conductivity σ and low thermal conductivity κ. However, it is difficult to modify one parameter without affecting the others due to their mutual dependence. Eventually, the Seebeck coefficient and electrical conductivity are strongly dependent on the charge carrier concentration[17,18], and influenced by the carrier mobility[19]. In most cases, the crucial parameter of the Seebeck coefficient is dominated by an energy-dependent electronic density of states (DOS) at the Fermi level in terms of the band theory[20,21].

Pure $BaTiO_3$ and $EuTiO_3$ are insulators with a band gap of ~3.2 eV[6] and ~1 eV[22], respectively. Their reduced forms $BaTiO_{3-\delta}$ and $EuTiO_{3-\delta}$ show n-type semiconducting behavior at high temperatures[23,24] . Sofo and Mahan[25] pointed out that semiconductors with a band gap of 10 k_BT_o are good thermoelectrics, k_B being the Boltzmann constant and T_o the operating temperature. Therefore,

from the band gap value determined by our DFT calculations (s. below), $Ba_{1-x}Eu_xTiO_{3-\delta}$ could be a promising material for thermoelectric power generation, when T_o is in the range of 1000 K < T < 1200 K (10 k_BT_o ~ 0.86 eV – 1 eV). In addition, utilizing magnetic semiconductors was proposed as an effective strategy to develop more efficient thermoelectric materials[26,27]. Thus, it is well worth to carry out careful thermoelectric property investigations on this material.

Similar to most of the $ATiO_3$ perovskites (e.g., $SrTiO_3$, $BaTiO_3$), the charge transfer gap of $EuTiO_3$ separates a valence band of filled oxygen 2*p* states and an empty conduction band of titanium 3*d* states[28,29]. However, a key difference of $EuTiO_3$ is the presence of a narrow and sharp Eu^{2+} 4*f* band localized at the top of the valence band[8,30], which is beneficial to a large Seebeck coefficient[24]. Subsequently, the localized Eu^{2+} 4*f* band is also introduced to form a new band structure in the Eu^{2+}-substituted $Ba_{1-x}Eu_xTiO_{3-\delta}$ compounds, which could result in different DOS according to the Eu^{2+} substitution content. On the other hand, due to the different ionic radii of 12-fold coordinated Eu^{2+}($r(Eu^{2+})$ = 1.59 Å, the value is extrapolated from the data given in literature[31]) and Ba^{2+}($r(Ba^{2+})$ = 1.75 Å)[31], the incorporation of smaller Eu^{2+} ion in $BaTiO_3$ unit cell could lead to distortion or tilting of the crystal structure, which could affect the DOS and phonon transport. Hence, the effect of the Eu^{2+} content on the electric transport properties and the charge carrier transfer mechanism in the $Ba_{1-x}Eu_xTiO_{3-\delta}$ compounds becomes an interesting question.

In this paper, we introduce a solution precursor route to synthesize the $Ba_{1-x}Eu_xTiO_{3-\delta}$ ($0.1 \le x \le 0.9$) powders with nano-sized particles. The crystal structure of the obtained powder samples was characterized and the thermoelectric properties of $Ba_{1-x}Eu_xTiO_{3-\delta}$ solid solution compounds were evaluated. A possible electron conduction mechanism for $Ba_{1-x}Eu_xTiO_{3-\delta}$ is discussed.

2. Experimental

2.1 Samples synthesis and preparation

A series of polycrystalline $Ba_{1-x}Eu_xTiO_{3-\delta}$ ($0.1 \le x \le 0.9$) samples was synthesized using a Pechini method followed by annealing under reducing conditions. The chemicals used for the experiment were europium(III) oxide (Alfa Aesar, 99.9%), barium acetate (Sigma-Aldrich, ≥ 99%), citric acid (Sigma-Aldrich, 99%), titanium(IV) bis (ammonium lactato) dihydroxide solution (Sigma-Aldrich, 50 wt. % in H_2O) and ethylene glycol (Sigma-Aldrich, ≥ 99%). The molar ratio of citric acid, ethylene glycol and the expected final product was set at 6:30:1. First, a stoichiometric amount of europium(III) oxide, barium

acetate and citric acid were weighted separately and placed into a round-bottom flask. Then an appropriate amount of distilled water was added and the mixture was heated to 373 K under vigorous magnetic stirring. Due to the fact that europium(III) oxide is insoluble in cold water but dissolves in citric acid aqueous solution, the white suspension slowly changed to a clear transparent solution in a few minutes. Subsequently, titanium (IV) bis (ammonium lactato) dihydroxide solution and ethylene glycol were added. After additional about 2 hours vigorous stirring at 338 K, the transparent solution was transferred to a pyrex crystallizing dish and heated in a muffle furnace at 473 K for 12 h followed by 753 K for 6 h. For crystallization, the obtained white precursors were annealed at 1273 K for 12 h in flowing forming gas (5 vol.% H_2 in Ar). The sample color gradually changed from dark gray to black with increasing europium concentration.

The disc-shaped bulk samples were prepared by cold isostatic pressing at ~ 205 MPa pressure to get the green compacted pellets followed by conventional ceramic sintering at $1473 \leq T \leq$ ~1673 K for 12 h under the identical conditions to the annealing process. The sintered disc samples were cut into rectangular bars (~ 10 × 3 × 2 mm^3) for electrical transport property measurements and square pellets (~ 8 × 8 × 2 mm^3) for the thermal diffusivity measurements.

2.2 Samples characterization

Powder X-ray diffraction (PXRD) data of all powder samples before and after sintering were collected by a Rigaku Smartlab X-ray diffractometer using Cu-$K\alpha_{1,2}$ radiation. Cu-K_β radiation was suppressed by a thin nickel foil with approximately 90 % efficiency. The diffraction patterns were recorded from 10° to 90° (2 theta) using continuous scanning at a step size of 0.01°. Rietveld refinements[32,33] were carried out using *FullProf* 2.k[34]. A pseudo-Voigt function was selected to describe the reflection profile. The background was treated by a 4th order polynomial function.

Synchrotron radiation powder diffraction was executed on the synthesized powder $Ba_{1-x}Eu_xTiO_{3-\delta}$ (x = 0.3, 0.5, 0.7) samples at 300 K at the ID22 beamline of the European Synchrotron Radiation Facility (ESRF) in Grenoble, France. The powder samples were loaded into 0.7 mm diameter Kapton® capillaries and mounted parallel to the axis of the diffractometer. Data were collected using both the high resolution setup (λ=0.32634(1) Å) for Ritveld refinement and a 2D CCD detector (Perkin Elmer XRD 1611CP3) for PDF analysis (λ=0.17712(1) Å). In this latter case,wavelength, sample-detector distance (379.3 mm), and azimuthal integration parameters were calibrated on a CeO_2 reference that was sintered for 4 h at 1673 K. The detector mask was created with the program FIT2D[35]; calibration and azimuthal integration were all done using the program pyFAI[36].

The average crystallographic structure was determined employing the Rietveld method[33], using the software GSAS[37]. Background was fitted by Chebyshev polynomials; absorption was corrected through the Lobanov empirical formula for the Debye-Scherrer geometry; line profiles were reproduced using a modified pseudo-Voigt function (function 3 in GSAS) accounting for asymmetry correction. In the last refinement cycles, scale factor, cell parameters, positional coordinates and atomic mean square displacements (MSD) were allowed to vary as well as background and line profile parameters.

Deviations from the long-range structure were studied by means of the PDF method. Analysis of the interatomic distances made use of the reduced Pair Distribution Function (PDF), G(*r*), which is the product of the sine Fourier transform of the experimental total scattering function, *S(Q)*, defined as[38]:

$$G(r) = 4\pi r[\rho(r) - \rho_0] = \frac{2}{\pi}\int_{Q_{min}}^{Q_{max}} Q[S(Q) - 1]\, sin(Qr)\, dQ \quad (1)$$

where $\rho(r)$ is the atomic pair density function and indicates the probability of finding an atom at a distance *r* from another atom, while ρ_0 is the atom number density. The G(*r*) function measures deviations from the average atomic density: a positive (negative) peak in the G(*r*) pattern indicates a range of *r* values whereby the probability of finding interatomic vectors is greater (lower) than that determined by the number density. G(*r*) curves were computed using the PDFgetX3 program[39] using data up to Q_{max} = 28.0 Å (where $Q = 4\pi \cdot \sin\theta/\lambda$ is the scattering vector). After background subtraction, the data were corrected for sample self-absorption, multiple scattering, and Compton scattering before Fourier transform finally yields the G(*r*) function. Structure refinements against the *G*(*r*) curves were carried out using the PDFGUI program[40]. The program assesses the accuracy of the refinement by the agreement factor (R_w) defined as follows[40]:

$$R_w = \left[\frac{\sum wi(G_i^{exp} - G_i^{calc})^2}{\sum wi(G_i^{exp})^2}\right]^{\frac{1}{2}} \quad (2)$$

Density functional theory (DFT) calculations were performed with the VASP (Vienna ab initio simulation package) code[41] using the Heyd-Scuseria-Ernzerhof (HSE) hybrid functional[42] for electronic exchange and correlation and a 8 × 8 × 6 k-point grid. Therefore, a $\sqrt{2} \times \sqrt{2} \times 2$ supercell of the cubic perovskite structure of $Ba_{1-x}Eu_xTiO_3$ was modelled . The supercell contains four formula unit cells and hence allows to tune *x* from 0, 0.25, 0.50, 0.75 to 1. The lattice constant and internal atomic positions were fully relaxed.

The content of metal ions (Eu, Ba, Ti) was determined by ICP-OES, the oxygen content was analyzed by carbothermal fusion using carrier gas hot gas extraction technique. Each measurement was repeated at least three times. The morphology of the annealed powders and the cross sections of

the sintered samples were characterized by scanning electron microscopy (SEM, Zeiss Merlin). Samples were sputtered with 1.5 nm iridium to enhance the conductivity on the surface.

The electrical resistivity (ρ) and the Seebeck coefficient (S) were measured simultaneously by a Seebeck coefficient / electric resistance measurement system (ZEM-3, Ulvac Riko) from ambient temperature to 1123 K in a forming gas atmosphere (5 vol.% H_2 in Ar). The uncertainty of the electrical resistivity and the Seebeck coefficient measurements is 3 %. The thermal conductivity (κ) was derived from experimental density (d), thermal diffusivity (λ) and specific heat capacity (C_p) values using the relationship:

$$\kappa = d \cdot \lambda \cdot C_P. \quad (3)$$

Experimental densities (d) of the bulk samples were determined by the Archimedes method. The thermal diffusivity (λ) was measured using a Netzsch LFA 457 laser flash analyzer in the temperature range of 300 K to 1173 K under a forming gas atmosphere (5 vol.% H_2 in Ar). The specific heat capacity (C_P) was calculated by the Dulong-Petit law $3NR/M$, where N is the number of moles including all atoms, R the gas constant (8.314 J/mol K) and M the molar mass of the compound (g/mol). The uncertainty of the thermal conductivity, specific heat capacity and density is 5 %, 5 % and 2 %, respectively. Accordingly, the uncertainty of the calculated ZT value results in 20 % by combining all those uncertainties.

3. Results and discussion

3.1 Crystal structure and microstructure

All synthesized powder samples were single phase, according to the collected PXRD data. The obtained reflections can be indexed in a cubic perovskite structure with space group $Pm\bar{3}m$, as shown in **Fig. 1(a)**. A weak reflection was observed for all samples at around $2\theta = 28.8°$, which results from the residual K_β radiation. Eu^{2+} substitution in $BaTiO_3$ results in unit cell contraction because the radius of Eu^{2+} is smaller than that of Ba^{2+}. Therefore, the XRD reflections regularly shift to higher diffraction angles, as shown in **Fig. 1(b)**. All as-prepared Eu^{2+}-substituted $BaTiO_3$ based compounds show a cubic perovskite structure at room temperature. The cubic perovskite structure was confirmed by synchrotron radiation diffraction measurements (s. below).

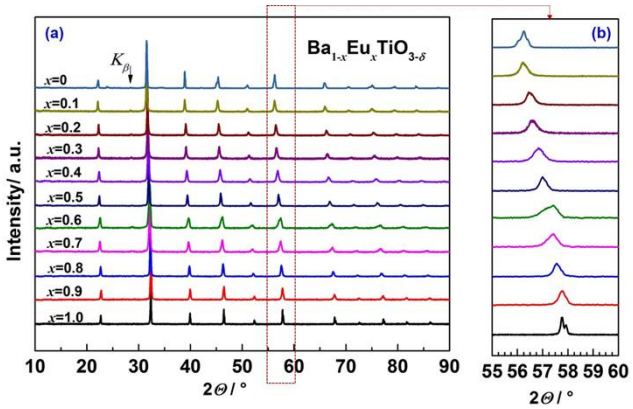

Figure 1. Powder X-ray diffraction patterns for synthesized $Ba_{1-x}Eu_xTiO_{3-\delta}$ ($0 \leq x \leq 1$) samples (a) and a zoom in XRD patterns (b). (all collected PXRD data contain a contribution of Cu-$K\alpha_2$)

The crystal structures of the samples have been refined by using the obtained PXRD raw data at ambient conditions. All refinement results are highly consistent with the proposed cubic structure model of perovskite-type $Ba_{1-x}Eu_xTiO_{3-\delta}$. **Fig. 2 (a)** and **(b)** present the refinement pattern of the sample x = 0.5 and the unit cell parameters depending on the Eu^{2+} concentration, respectively. The unit cell parameter decreases linearly with increasing Eu^{2+} concentration following Vegard's law. The unit cell parameter of $BaTiO_3$ obtained by DFT calculations was 3.99 Å. Upon increasing Eu^{2+} concentration it decreased to a value of 3.91 Å for $EuTiO_3$, which is in excellent agreement with experimental values.

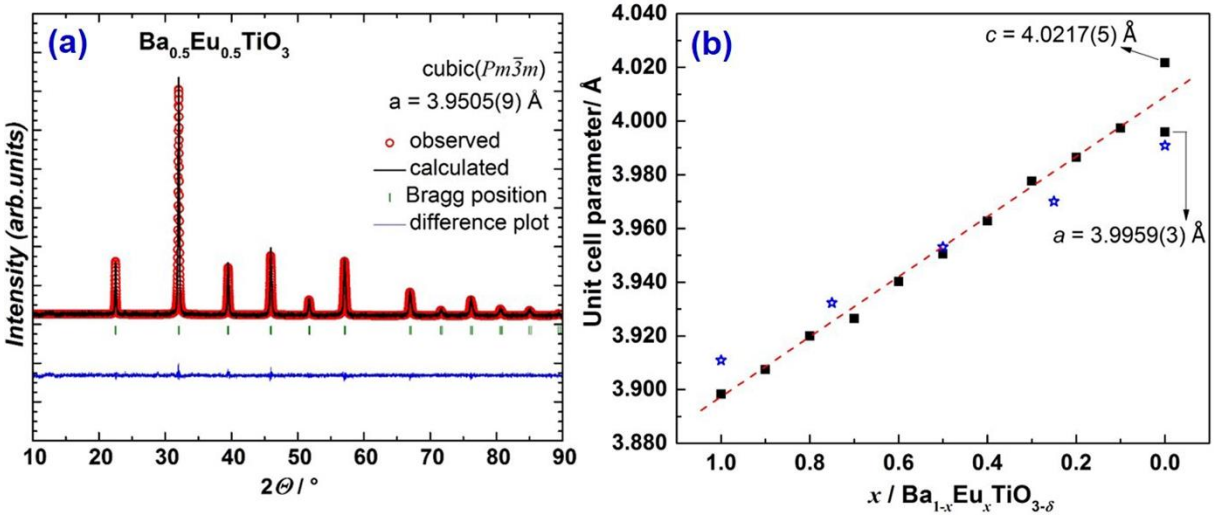

Figure 2. Powder X-ray diffraction refinement pattern of sample $Ba_{0.5}Eu_{0.5}TiO_{3-\delta}$ (a) and the unit cell parameter as a function of the Eu^{2+} concentration, the star symbol denotes the unit cell parameters calculated by DFT (b).

The chemical compositions of all samples are summarized in **Table 1**. The cation ratio for all samples was in good agreement with the nominal composition. In addition, all samples showed oxygen deficiency due to the reducing atmosphere used during both the synthesis and the sintering process. There is no clear relationship between the oxygen deficiency and Eu^{2+} content. Nevertheless, in this study, the effect of oxygen content on the TE properties can be neglected at high temperature (T > 783 K) compared to that of Eu^{2+} content, which will be discussed later in more detail.

Table 1. Experimental composition, refined unit cell parameter (a), experimental bulk density (d), relative density (ξ), porosity (ε) of the sintered bulk $Ba_{1-x}Eu_xTiO_{3-\delta}$ ($0.1 \leq x \leq 0.9$) samples. Estimated standard deviations (ESDs) are given in brackets.

Sample No.	Experimental composition				a/ Å	d/ g/cm³	ξ*/ %	ε/ %
	Eu	Ba	Ti	O				
x = 0.1	0.100(1)	0.892(8)	1.01(1)	2.89(3)	3.9973(4)	5.27	86	14
x = 0.2	0.207(3)	0.795(8)	1.03(1)	2.92(3)	3.9865(3)	5.55	90	10
x = 0.3	0.297(3)	0.704(7)	1.00(1)	2.87(3)	3.9776(6)	5.78	91	9
x = 0.4	0.387(4)	0.604(6)	1.01(1)	2.97(3)	3.9627(8)	6.07	95	5
x = 0.5	0.499(7)	0.513(5)	1.01(1)	2.93(3)	3.9505(9)	5.97	93	7
x = 0.6	0.604(7)	0.387(3)	1.00(1)	2.95(3)	3.9402(7)	6.17	94	6
x = 0.7	0.692(8)	0.307(4)	1.01(1)	2.95(3)	3.9264(3)	6.37	97	3
x = 0.8	0.793(8)	0.205(4)	1.03(1)	2.97(3)	3.9199(6)	5.69	84	16
x = 0.9	0.900(5)	0.104(1)	1.02(1)	2.86(3)	3.9074(3)	5.92	86	14

*Theoretical densities are obtained by XRD refinement calculation.

Synchrotron radiation diffraction data of the selected samples (x = 0.3, 0.5, 0.7) collected at ambient temperature allows some insight into the structure of $Ba_{1-x}Eu_xTiO_{3-\delta}$ compounds at different length scales. SR-PXRD data have been first analysed through the Rietveld method. **Fig. 3 (a)** shows the fit of the x = 0.5 sample, while the refined structural parameters for all the solid solutions are reported in **Table 2**.

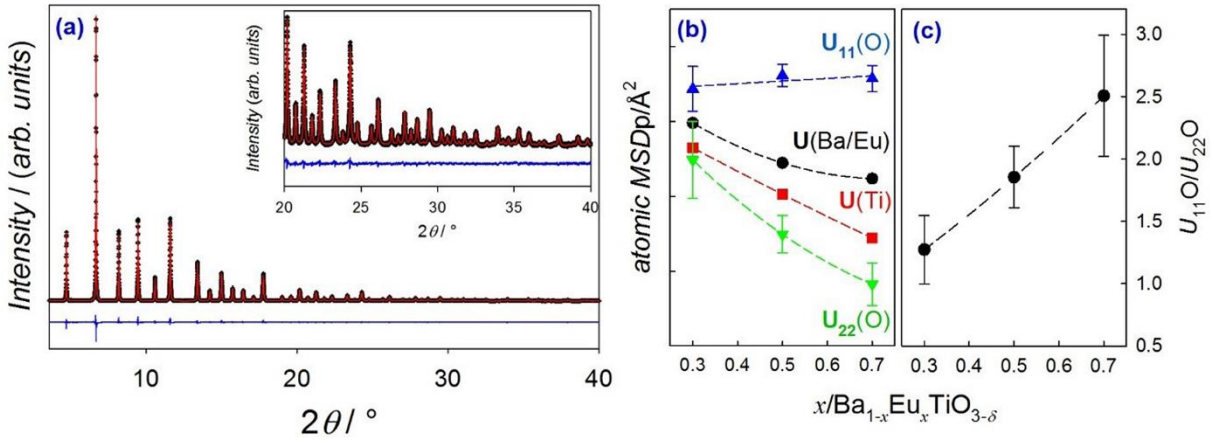

Figure 3. (a) PXRD pattern of $Ba_{0.5}Eu_{0.5}TiO_{3-\delta}$. Measured (black crosses) and calculated (red line) profiles are shown as well as residuals (blue line). The inset highlights the high 2θ range. (b) U(Eu/Ba), U(Ti), U_{11}(O) and U_{22}(O) mean square displacement parameters (MSDp) represented as black circles, red squares, blue triangles up, green triangles down, respectively. (c) U_{11}(O)/U_{22}(O) ratio at 90 K.

Table 2. Rietveld refinement results referring to $Ba_{1-x}Eu_xTiO_{3-\delta}$ samples. Atomic positions are Ti (0, 0, 0), Ba/Eu (½, ½ ½) and O (0, ½, 0). The atomic MSD parameters U are expressed in Å^2. Please note that Ba/Eu and Ti MSDp are isotropic because of symmetry constrains.

Sample No.	a/ Å	U				R_p	$R(F^2)$
		U(Ba/Eu)	U(Ti)	$U_{11/33}$(O)	U_{22}(O)		
x = 0.3	3.98047(3)	0.00796(8)	0.0073(1)	0.0089(6)	0.0070(10)	0.0437	0.0339
x = 0.5	3.95372(8)	0.00689(3)	0.00605(7)	0.0092(3)	0.0050(5)	0.0337	0.0244
x = 0.7	3.93198(2)	0.00647(4)	0.00488(7)	0.0092(4)	0.0037(6)	0.0400	0.0212

The Rietveld analysis of high-resolution PXRD data shows that all the investigated $Ba_{1-x}Eu_xTiO_3$ solid solutions have an undistorted cubic perovskite-type structure (space group $Pm\bar{3}m$) at T = 300 K. Consistent with the laboratory PXRD data. The volume occupied by one formula unit of $Ba_{1-x}Eu_xTiO_{3-\delta}$ decreases linearly according to the smaller ionic radius of Eu^{2+} with respect to Ba^{2+}.

The atomic mean square displacement parameters (MSDp) U are strongly related to the disorder status of these solid solutions[43,44]. **Fig. 3 (b)** reports the dependence of U(Eu/Ba), U(Ti), U_{11}(O), and U_{22}(O) on the Eu^{2+} concentration. In the oxygen anisotropic MSD tensor U_{22}(O) is along the Ti–O–Ti bond and U_{11}(O) ($\equiv U_{33}$(O)) perpendicular to it. A steep decrease of the U_{11}(O)/U_{22}(O) ratio is observed as the sample becomes richer in Ba^{2+} (**Fig. 3 (c)**), because U_{22}(O) increases while U_{11}(O) remains nearly constants (**Fig. 3 (b)**). This ratio should be much larger than 1 in absence of any disorder, because the

potential energy surface normally rises more steeply along the Ti–O bond direction than in the direction perpendicular to it. The decreasing ratio suggests a broader distribution of the Ti–O bonds along the bonding direction, probably by imitating the off-centering of Ti^{4+} and Eu^{2+}/Ba^{2+} as known from $BaTiO_3$. The disorder picture was further investigated by PDF analysis of the 2D data of the same sample aliquots. PDF analysis revealed a clear mismatch between short-range structure and the long-range crystallographic phase of $Ba_{1-x}Eu_xTiO_{3-\delta}$.

G(*r*) of any sample was not adequately reproduced by the cubic long-range structure model in the short-range region (2.4 ≤ *r* ≤ 8 Å, see **Fig. 4 (a-c)**). Symmetry lowering taking into account polar distortion modes as in $BaTiO_3$[45]and non-polar modes as in $EuTiO_3$[46], respectively, was tested. *G*(*r*) fits in the range evidenced a small magnitude of structural distortion compared with other disordered perovskites[47,48]. However, a simple model based on one of the possible symmetry breaking of $Pm\bar{3}m$ was not able to reproduce the short-range order while models combing polar and non-polar modes (e.g. *Ima*2, *R*3*c*)) led to overparametrised fits. The most suitable model for the *G*(*r*) of all three samples was an *Amm*2 phase (**Fig. 4 (d-f)**). This model reflects the long-range structure of pure $BaTiO_3$ at RT[49] and allows for a movement of both Ti^{4+} and Ba^{2+}/Eu^{2+} along the <110> direction of the parent cubic cell (**Fig. 4 (d-f)**), while an *I*4/*mcm* model like in $EuTiO_3$ only accounts for the rotation of the octahedral network. Additionally, the *Amm*2 model allows for the emergence of uniformly oriented electric dipoles[45][Comment] (see Supporting Information). The variation of the composition clearly revealed the involvement of the TiO_6 octahedra and the Ba/EuO_{12} cuboctahedra. For $x = 0.7$ the cuboctahedron is most distorted as evidenced by the change of the Ba–O–Ba angle from 158.6° to 156.9°. Conversely, the TiO_6 octahedra become more regular as expressed by Baur's distortion index *D*[50], where D is standard deviation of the Ti-O distances distribution, (see **Fig. 4 (g-i)**) as it was observed above from the MSD parameters.

The agreement between data and the $Pm\bar{3}m$ model gradually improves in successive fits covering farther distances in real space (8 ≤ *r* ≤ 40 Å). This gives an indication about the nanometer coherence length of disorder in $Ba_{1-x}Eu_xTiO_{3-\delta}$ (**Fig. 4 (j-l)**). As **Fig. 4 (m-o)** evidences, the disordered *Amm*2 model and the cubic model are practically equivalent in the *r* > 20 Å range. Thus, since the symmetry breaking of $Pm\bar{3}m$ symmetry is confined to the nanometer scale, it can be inferred that local distortions with different orientations coexist in the same crystallite, preserving the long-range cubic symmetry[44].

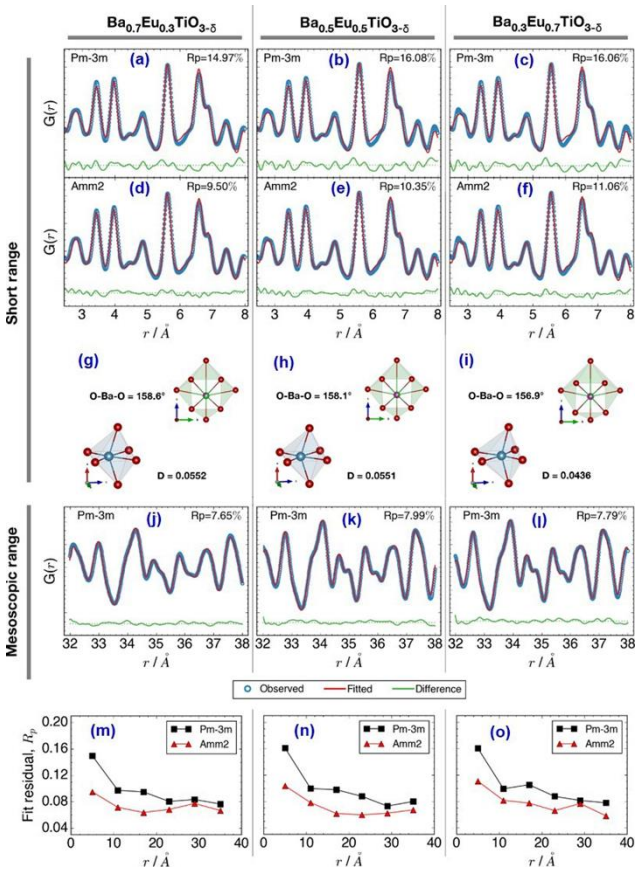

Figure. 4. (a)-(f) and (j)-(l) $G(r)$ functions of $Ba_{1-x}Eu_xTiO_{3-\delta}$ at different length scales and using different models. Measured (empty circles) and calculated (red line) $G(r)$ are shown as well as residuals (red line). The used space group and the residual parameter *Rp* of the refinements are written at the top of each panel. In (g)-(i) the distortions of Ti and Eu/Ba oxygen cages are depicted as sketches. *D* is the Baur's distortion index[50]. (m)-(o) report the *Rp* of fits at different *r* intervals (each 8 Å wide).

Fig. 5 shows SEM images of a synthesized powder sample as well as a cross section of its corresponding sintered bulk sample for the compound $Ba_{0.5}Eu_{0.5}TiO_{3-\delta}$. As all synthesized powder samples, the illustrated sample has a homogeneous morphology and a particle size of around 40 nm (**Fig. 5 (a)** and **(b)**). The amorphous precursor underwent crystallization during the annealing process at 1273 K for 12 h leading to well crystallized nanocrystals. The well-sintered bulk sample possessing high density with closed pores is clearly recognizable in **Fig. 5(c)** and **(d)**. The bulk density and porosity are listed in **Table 1.** Assuming that the pores are spherical and homogeneously distributed in the dense bulk samples, the experimental electrical conductivity data and thermal conductivity data could be corrected with the Maxwell equation[51,52] for discussion. Because obvious cracks were observed in the

samples x = 0.1 and 0.3, the thermoelectric transport properties of these two samples were not taken into account in this study.

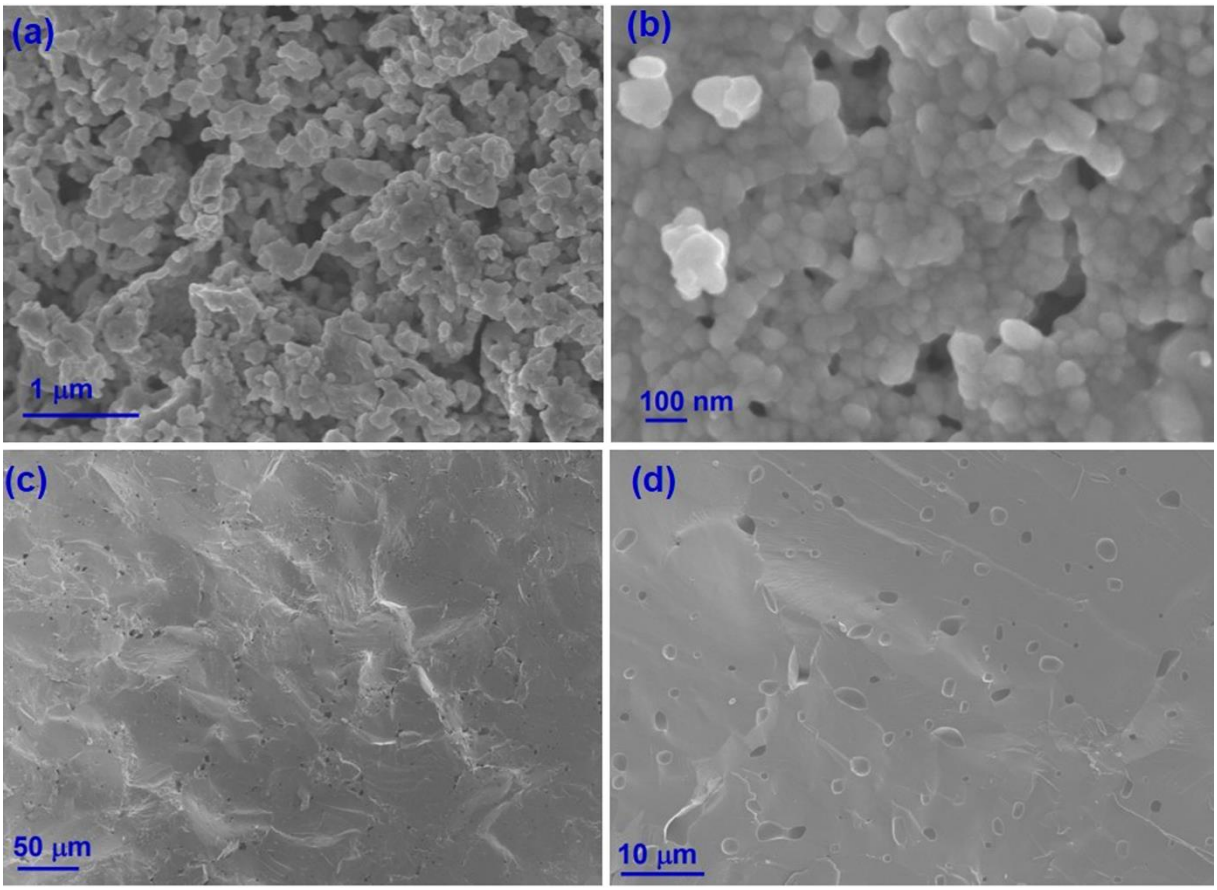

Figure 5. SEM images of a synthesized powder sample (a) (b) and cross section of its corresponding well-sintered bulk sample (c) (d) for $Ba_{0.5}Eu_{0.5}TiO_{3-\delta}$ composition.

3.2 Electrical transport properties

The temperature dependence of the Seebeck coefficient S of the sintered bulk samples $Ba_{1-x}Eu_xTiO_{3-\delta}$ (x = 0.2, 0.4, 0.5, 0.6, 0.7, 0.8 and 0.9) in the temperature range of 300 K < T < 1200 K is presented in **Fig. 6**. The values are negative in the entire measured temperature range, indicating that the dominant charge carriers are electrons. The S of $Ba_{0.1}Eu_{0.9}TiO_{3-\delta}$ is around 850 μVK^{-1} at 323 K and the absolute value $|S|$ decreases with increasing temperature, which is in accordance with the reported data of pristine $EuTiO_{3-\delta}$[53] (dashed line with open circles in **Fig. 6**). The S of n-type semiconductors can be calculated by the following equation[54]:

$$S = \frac{-k_B}{e}\left(\frac{(r+2)F_{r+1}(\xi)}{(r+1)F_r(\xi)} - \xi\right) \quad (4)$$

where k_B is the Boltzmann constant, e the electron charge, ξ the chemical potential, r the scattering parameter of the relaxation time, and F_r the Fermi integral given by

$$F_r(\xi) = \int_0^\infty \frac{x^r}{1+e^{x-\xi}} dx \quad . \tag{5}$$

|S| monotonically decreases with increasing temperature due to a decrease of the Fermi integral with temperature. At low temperatures, there is no well-defined relation between Eu^{2+} substitution content and the value of S of $Ba_{1-x}Eu_xTiO_{3-\delta}$; however, at high temperatures (T > 1000 K), S measurably decreases with enhanced Eu^{2+} content. In addition, the S values of $Ba_{1-x}Eu_xTiO_{3-\delta}$ are much less dependent on the temperature (T > 1000 K), suggesting that the kinetic terms of S can be neglected and the behavior of S can be described by Heikes formula[55]. $Ba_{1-x}Eu_xTiO_{3-\delta}$ compounds are considered to belong to strongly correlated electron systems[46,56,57] with a large on-site Coulomb repulsion parameter U[56,58]. Consequently, S can be estimated by the following modified Heikes formula[59]:

$$S(T \to \infty) = \frac{-k_B}{e} \ln \frac{2(1-n)}{n} \tag{6}$$

where n is the charge carrier concentration per unit cell. By this means, the charge carrier concentration of $Ba_{1-x}Eu_xTiO_{3-\delta}$ can be calculated from the measured S values of $Ba_{1-x}Eu_xTiO_{3-\delta}$ at 1123 K. The results summarized in **Table 3** show that the charge carrier concentration increases with increasing Eu^{2+} concentration. This trend can be ascribed to the Eu 4*f* electrons, which will be discussed in more detail below.

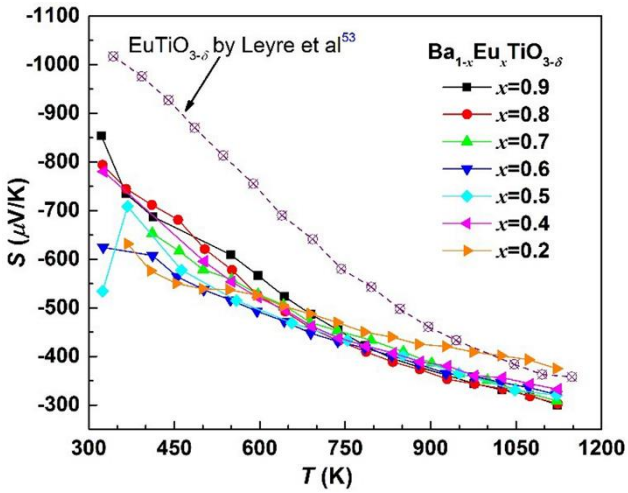

Figure 6. Temperature dependence of the Seebeck coefficient S of sintered bulk samples $Ba_{1-x}Eu_xTiO_{3-\delta}$

The electrical conductivity of the sintered $Ba_{1-x}Eu_xTiO_{3-\delta}$ (x = 0.2, 0.4, 0.5, 0.6, 0.7, 0.8 and 0.9) samples as a function of temperature is shown in **Fig. 7(a)** and **(b)**. The conductivity increases with

increasing temperature for all samples, exhibiting semiconducting behavior in the whole measured temperature range. The electrical conductivity exponentially increases between room temperature and about 470 K (see **Fig. 7(b)**), implying that electrons (main charge carriers) are excited from donor levels originating from Ti^{3+} or oxygen vacancies located below the bottom of the CB[60,61,62] into the conduction band in this temperature range[20,21]. At higher temperatures (T > 783 K), the electrical conductivity rapidly increases with increasing temperature. This can be ascribed to intrinsic excitation where the thermal energy is sufficient to excite electrons from the valence band to the conduction band. Also, the electrical conductivity of $Ba_{1-x}Eu_xTiO_{3-\delta}$ increases with the Eu^{2+} content at higher temperatures. This is consistent with the influence of Eu^{2+} substitution on the Seebeck coefficient at higher temperatures.

The calculated total DOS of $Ba_{1-x}Eu_xTiO_3$ (x = 0, 0.25, 0.5, 0.75, 1) is shown in **Fig. 8.** The results revealed that $BaTiO_3$ has in accordance with literature reports[6,63] an energy gap of 3.2 eV between filled oxygen 2*p* states and empty Ti 3*d* states. Similar as previously reported[6,24,63,64] for $EuTiO_3$ an energy gap of 0.9 eV between filled Eu 4*f* (leading to a magnetic moment of 7 μ_B) and empty Ti 3*d* states was observed. For $Ba_{1-x}Eu_xTiO_3$ (x > 0) narrow and sharp Eu^{2+} 4*f* states were present in the original band gap of $BaTiO_3$. With increasing Eu^{2+} content the intensity of the Eu^{2+} 4*f* DOS increased as expected. The results of the DOS calculations of $Ba_{1-x}Eu_xTiO_3$ were highly consistent with the experimental data observed for the Seebeck coefficient and electrical conductivity measurements. This is especially obvious for two features: (i) the energy gap is almost unchanged from the Eu^{2+} substitution level; (ii) the carrier density per unit cell of the filled Eu 4*f* is proportional to the Eu^{2+} concentration. In principle, in the whole compositional and temperature range of this $Ba_{1-x}Eu_xTiO_3$ (x > 0) system electrons as charge carriers can be donated by either oxygen vacancies (not included in the DOS calculation model) or by the filled Eu^{2+} 4*f* levels. At high temperatures (T > 783 K), the electron transitions from Eu 4*f* to Ti 3*d* become dominant for conduction, which plays a central role in the improvement of the electrical conductivity[65]. Thus, it was concluded that the charge carrier concentration n became proportional to x, qualitatively consistent with the experimental results shown in **Table 3**.

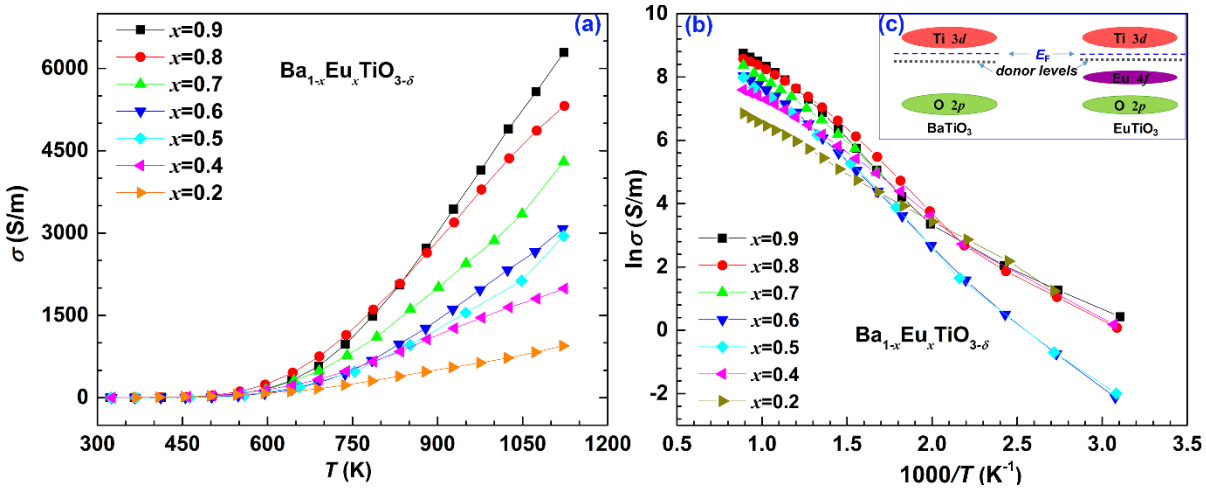

Figure 7. Temperature dependence of the electrical conductivity of sintered $Ba_{1-x}Eu_xTiO_{3-\delta}$ bulk samples (a) and (b), and the schematic diagram of the band structures of $BaTiO_3$ and $EuTiO_3$ (c).

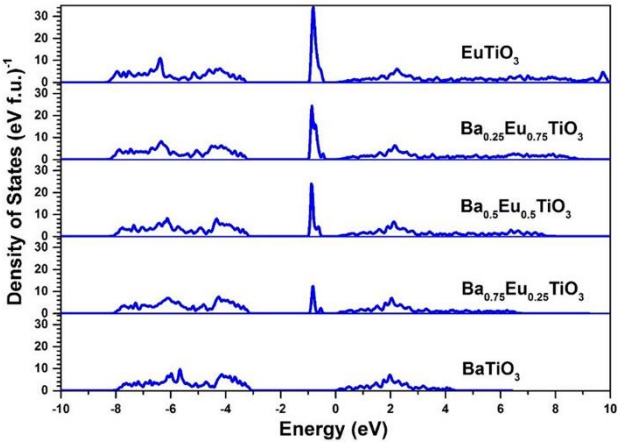

Figure 8. Calculated total density of states (DOS) of $Ba_{1-x}Eu_xTiO_3$ (x = 0, 0.25, 0.5, 0.75, 1).

In order to further investigate the dominant transport mechanism (thermal disorder, polaron hopping etc.) of $Ba_{1-x}Eu_xTiO_{3-\delta}$, the activation energies were quantified according to the model of Mott's adiabatic small polaron conduction[66]. $\rho(T)$ and $S(T)$ curves are fitted by the formula[67]

$$\rho(T) = \rho_0 \exp\left(\frac{E_A}{k_B T}\right) \tag{7}$$

and

$$S = \frac{k_B}{e}\left(\frac{E_S}{k_B T} + r\right) , \tag{8}$$

where E_A is the activation energy determined from the resistivity $\rho(T)$ measurement, E_S is the thermopower activation energy, ρ_0 as well as r are constants. Both the $\rho(T)$ and the $S(T)$ curves were fitted in the same temperature range, and the results are illustrated in **Fig. 9** by solid lines. When E_A is

larger than E_S, thermally activated hopping with a hopping binding energy $W_p = 2(E_A - E_S)$ occurs[66,67]. The activation energies are calculated and listed in **Table 3**. The values of both E_A and E_S depend on the Eu^{2+} content, and the dependence behavior of E_A and E_S is similar. When $x \leq 0.6$, E_A is larger than E_S indicating that the dominating conduction mechanism belongs to polaron conduction. The small polaron hopping nature of $BaTiO_3$ was already clarified by Ihrig et al[68]. Whereas, when $x > 0.6$, E_A is not larger than E_S implying the dominating conducting mechanism of $Ba_{1-x}Eu_xTiO_{3-\delta}$ system changes from polaron hopping conduction into thermally activated band conduction, which is consistent with $EuTiO_3$[24]. PDF measurements showed that a decrease of the distortion of the TiO_6 octahedron is concomitant to the switching of the conduction regime suggesting that the local Ti environment should affect the polaron binding energy.

The carrier mobility (μ) of $Ba_{1-x}Eu_xTiO_{3-\delta}$ was calculated using the relation $\sigma = ne\mu$, where σ is the measured electrical conductivity and n is carrier concentration estimated by Heikes formula (see equation (6)). The results are illustrated in **Fig. 10** as a function of the Eu^{2+} content. The calculated μ values of as-prepared $Ba_{1-x}Eu_xTiO_{3-\delta}$ compounds are in the same order of magnitude as reference data of $BaTiO_3$ (0.1 – 0.5 $cm^2V^{-1}s^{-1}$)[68], and reveal that the carrier mobility of samples with band conduction ($x > 0.6$) was higher than that of samples with a polaron hopping mechanism ($x \leq 0.6$).

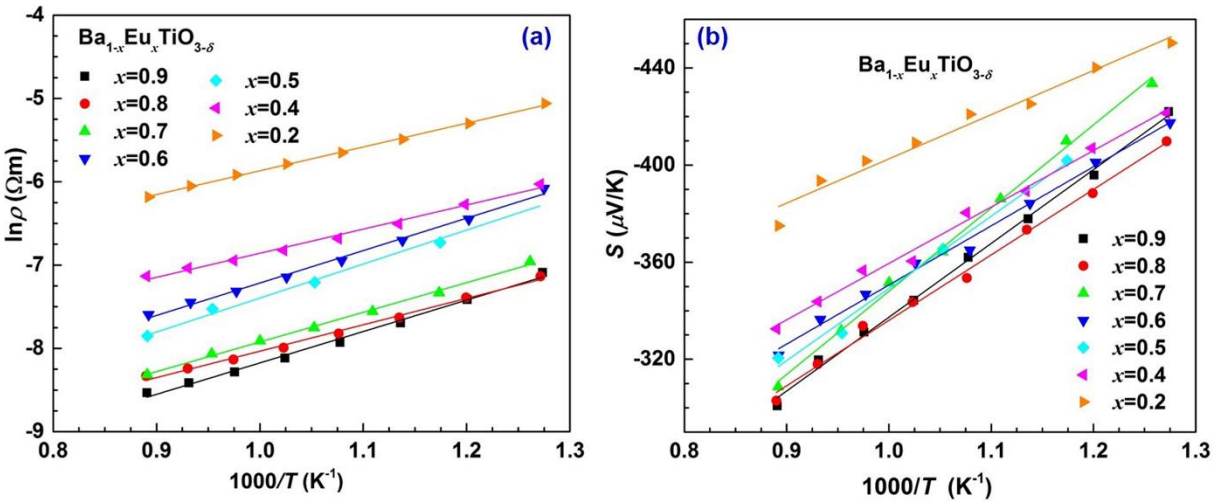

Figure 9. Plot of lnρ (a) and S (b) of $Ba_{1-x}Eu_xTiO_{3-\delta}$ samples as a function of the inverse temperature.

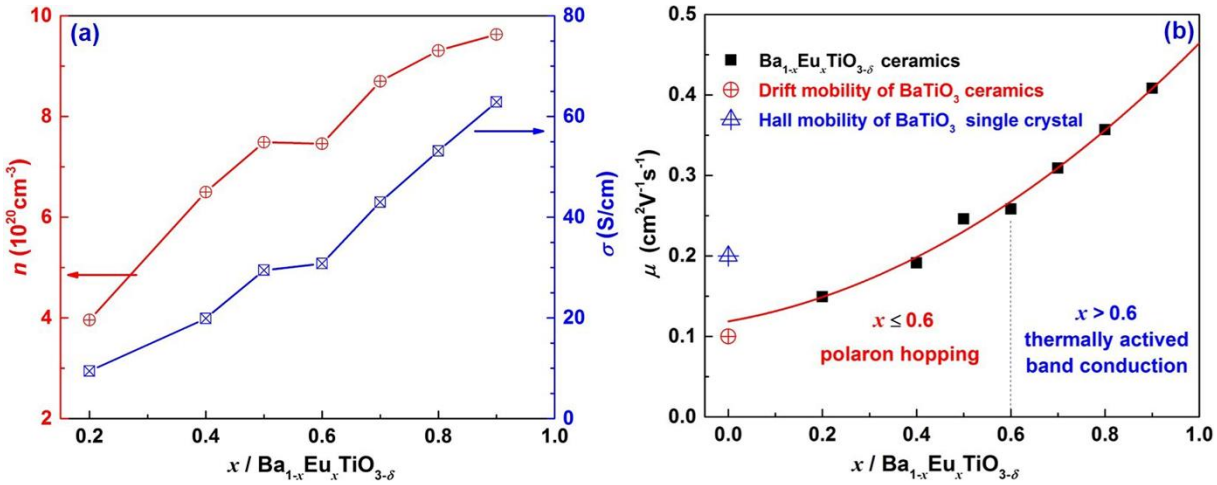

Figure 10. Calculated charge carrier concentration n and electrical conductivity σ (a), and carrier mobility μ (b), as a function of the Eu^{2+} content x at 1123 K.

Table 3. Electrical conductivity σ, Seebeck coefficient S, activation energies E_A and E_S, polaron binding energy W_p, charge carrier concentration n and mobility μ of all measured samples at 1123 K.

Samples No.	$\sigma_{1123\,K}$ (S/m)	E_A (eV)	S_{1123K} (μV/K)	E_s (eV)	W_p (eV)	$n_{1123\,K}$ (×10^{20} cm^3)	μ ($cm^2V^{-1}s^{-1}$)
x = 0.2	945	0.24	-375	0.18	0.12	4.0	0.15
x = 0.4	1990	0.24	-332	0.23	0.02	6.5	0.19
x = 0.5	2948	0.33	-320	0.30	0.06	7.5	0.25
x = 0.6	3081	0.32	-321	0.24	0.16	7.5	0.26
x = 0.7	4300	0.29	-308	0.34	-	8.7	0.31
x = 0.8	5317	0.26	-302	0.27	-	9.3	0.35
x = 0.9	6289	0.30	-300	0.30	-	9.6	0.41

The power factor ($PF = S^2\sigma$) is primarily a measure of the electrical properties of a thermoelectric material. The PF values of $Ba_{1-x}Eu_xTiO_{3-\delta}$ are shown in **Fig. 11**. Eu^{2+} substitution significantly enhances PF of $Ba_{1-x}Eu_xTiO_{3-\delta}$, resulting from a particularly strong improvement of the electrical conductivity with Eu^{2+} substitution. The highest PF of 0.55 mW/mK^2 is achieved for $Ba_{0.1}Eu_{0.9}TiO_{3-\delta}$ at 1070 K, which is by a factor of 4 higher compared to $Ba_{0.8}Eu_{0.2}TiO_{3-\delta}$.

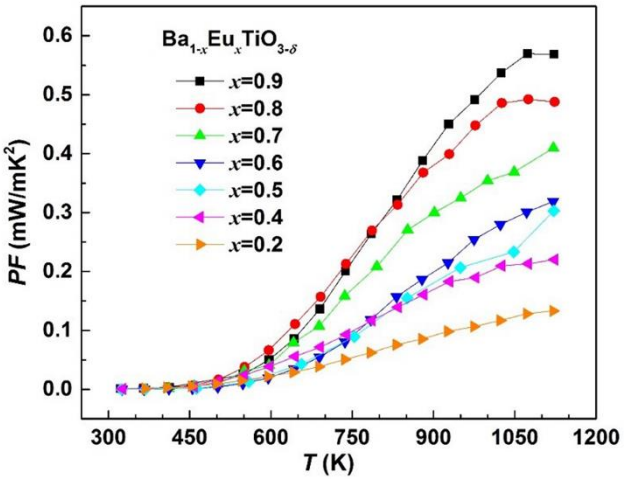

Figure 11. Temperature dependence of the power factor (*PF*) of $Ba_{1-x}Eu_xTiO_{3-\delta}$ samples.

3.3 Thermal transport properties and *ZT*

The temperature dependence of the thermal conductivity (κ) of $Ba_{1-x}Eu_xTiO_{3-\delta}$ is shown in **Fig. 12(a)**. At room temperature, κ generally increases with europium content *x*. The lattice thermal conductivity (κ_L) can be estimated from the equation $\kappa = \kappa_L + \kappa_e$. The electrical thermal conductivity κ_e can be derived from the Wiedemann-Franz relation, $\kappa_e = L_0\sigma T$, where L_0 is the Lorenz number. L_0 of degenerate systems is usually estimated at 2.45×10^{-8} V^2K^{-2}, although it depends on the Fermi energy, the band structure and the scattering process[69]. Since the electrical conductivity of all $Ba_{1-x}Eu_xTiO_{3-\delta}$ samples is quite low (highest value ~ 6×10^3 S/m), the calculated κ_e values account for less than 7 % of the total thermal conductivity; thus, it is reasonable to assume that $\kappa \approx \kappa_L$. In the whole measured temperature range, κ_L of all $Ba_{1-x}Eu_xTiO_{3-\delta}$ compounds follows a T^{-1} dependence, indicating that the dominant phonon scattering mechanism in all $Ba_{1-x}Eu_xTiO_{3-\delta}$ compounds is the Umklapp scattering (phonon–phonon interactions). The dependence of κ_L on the Eu^{2+} content *x* of all $Ba_{1-x}Eu_xTiO_{3-\delta}$ compounds at 323 K and 1123 K is plotted in **Fig. 12 (b)**. In a solid solution system, the lowest lattice thermal conductivity is usually associated with the highest disorder due to the mass fluctuation and point defect scattering. However, κ_L of the $Ba_{1-x}Eu_xTiO_{3-\delta}$ compounds increased with increasing Eu^{2+} content. Similar results were previously obtained for the $BaTiO_3$–$SrTiO_3$ solid solution[70,71,71]. In accordance with PDF results, a possible interpretation of this finding is that Eu^{2+} substitution leads to a reduction of the Ti–O average distance and increase of TiO_6 distortion, which strengthens the Ti–O bond. The available literature data[72] suggest that stronger Ti–O bonds lead to a higher κ_L. In the studied system, the effect of the bond strength on the thermal conductivity appears to dominate over simultaneously occurring

point defect scattering. In order to prove this theory, theoretical calculations on how the Ti–O bond length affects the lattice thermal conductivity of the $BaTiO_3$–$EuTiO_3$ solid solution should be conducted.

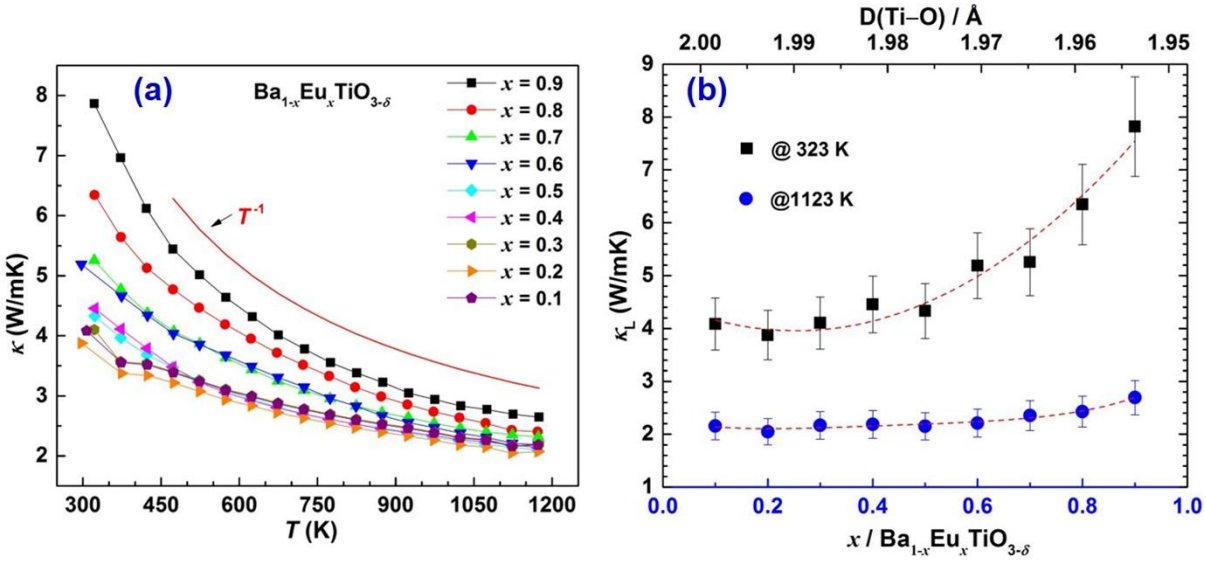

Figure 12. Temperature dependence of the thermal conductivity κ (a) and the lattice thermal conductivity κ_L (b) of $Ba_{1-x}Eu_xTiO_{3-\delta}$ as a function of the Eu^{2+} content x and Ti–O distance at 323 K and 1123 K.

The calculated dimensionless figure-of-merit (ZT) is shown in **Fig. 13**. The ZT of all samples monotonically increases with increasing temperature and reaches the highest value at the highest measured temperature T = 1123 K. Although Eu^{2+} substitution raises the thermal conductivity, the ZT value of the $Ba_{1-x}Eu_xTiO_{3-\delta}$ compounds significantly increase with increasing Eu^{2+} contents at T > 650 K, owing to remarkable Eu^{2+}-induced improvement of electrical conductivity at high T. The highest ZT value of 0.24 was obtained at 1123 K for the Eu^{2+}-richest compound, $Ba_{0.1}Eu_{0.9}TiO_{3-\delta}$.

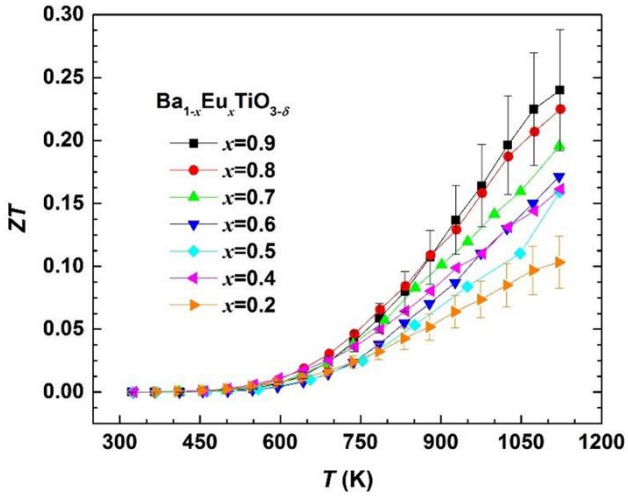

Figure 13. Temperature dependence of *ZT* of $Ba_{1-x}Eu_xTiO_{3-\delta}$ samples.

Although the highest observed thermoelectric performance is noticeably lower than that attained for some $SrTiO_3$-based materials[73,74,74], the results provide a clear insight on how electrical properties can be significantly improved through introducing the filled Eu^{2+} 4*f* levels in the electronic band structure. Further approaches for enhancing the thermoelectric performace in the discussed materials may include complementary engineering of the defect structure[75], by controlled indroducing the oxygen vacancies, which may simultaneously act as efficient phonon scatterers and electron donors, and cation vacancies, aiming to increase the charge carrier mobility.

4. Conclusions

Single phase Eu^{2+}-substituted $Ba_{1-x}Eu_xTiO_{3-\delta}$ compounds were successfully synthesized via a Pechini method followed by annealing and sintering under reducing conditions. The effects of Eu^{2+} substitution on the thermoelectric transport properties of $Ba_{1-x}Eu_xTiO_{3-\delta}$ were systematically investigated. Rietveld refinements of PXRD data revealed a cubic perovskite structure of all $Ba_{1-x}Eu_xTiO_{3-\delta}$ ($0.1 \leq x < 1$) samples. The lattice parameter linearly decreases with increasing Eu^{2+} content in accordance with Vegard's law. However, local polar distortions detected by PDF analysis with a coherence length of ≈ 1 – 2 nm coexist with the cubic structure in the solid solutions. Calculation of the DOS predicted a significant reduction of the band gap and an increase of the electrical conductivity by partial substitution of Ba^{2+} with Eu^{2+} in $BaTiO_3$. Indeed, in great accordance in the experimental data with increasing Eu^{2+} contents, the electrical conductivity of $Ba_{1-x}Eu_xTiO_{3-\delta}$ increased significantly. The observed Seebeck coefficient is negative (*n*-type semiconductor) and exhibits an opposite trend at high temperature in

comparison with the electrical conductivity. Although Eu^{2+} substitution slightly decreases the Seebeck coefficient and enhances the thermal conductivity, the remarkable enhancement of electrical conductivity makes $Ba_{1-x}Eu_xTiO_{3-\delta}$ ($0 < x < 1$) appear promising for high temperature ($T > 1000$ K) thermoelectric applications.

Acknowledgments

This research was supported by Deutsche Forschungsgemeinschaft through the DFG Priority Program SPP 1386 (Grant WE 2803/2-2). The authors are grateful to the MPI-FKF Nanostructuring Lab (Prof. Dr. Jürgen Weis) for the opportunity to use the SEM facility and to the European Synchrotron Radiation Facility (ESRF) for provision of beam time. They are also greatly indebted with Dr. Mauro Coduri for kind assistance in using the ID22 beamline. Dr. A.V. Kovalevsky acknowledges the support of FCT (projects UID/CTM/50011/2013 and IF/00302/2012). Finally, we want to thank Dr. Angelika Veziridis for intensive discussions on the manuscript.

References

1 K. J. Choi, M. Biegalski, Y. L. Li, A. Sharan, J. Schubert, R. Uecker, P. Reiche, Y. B. Chen, X. Q. Pan and V. Gopalan, *Science*, 2004, **306**, 1005–1009.

2 S. Wada, K. Yako, H. Kakemoto, T. Tsurumi and T. Kiguchi, *Journal of Applied Physics*, 2005, **98**, 14109.

3 S. Roberts, *Physical Review*, 1947, **71**, 890.

4 R. Landauer, *Journal of Applied Physics*, 1957, **28**, 227–234.

5 D. C. Sinclair and A. R. West, *Journal of Applied Physics*, 1989, **66**, 3850–3856.

6 S. H. Wemple, *Physical Review B*, 1970, **2**, 2679.

7 T. R. McGuire, M. W. Shafer, R. J. Joenk, H. A. Alperin and S. J. Pickart, *Journal of Applied Physics*, 1966, **37**, 981–982.

8 H. Akamatsu, Y. Kumagai, F. Oba, K. Fujita, H. Murakami, K. Tanaka and I. Tanaka, *Physical Review B*, 2011, **83**, 214421.

9 J. H. Lee, L. Fang, E. Vlahos, X. Ke, Y. W. Jung, L. F. Kourkoutis, J.-W. Kim, P. J. Ryan, T. Heeg and M. Roeckerath, *Nature*, 2010, **466**, 954–958.

10 K. J. Choi, M. Biegalski, Y. L. Li, A. Sharan, J. Schubert, R. Uecker, P. Reiche, Y. B. Chen, X. Q. Pan and V. Gopalan, *Science*, 2004, **306**, 1005–1009.
11 T. Katsufuji and H. Takagi, *Physical Review B*, 2001, **64**, 54415.
12 D. L. Janes, R. E. Bodnar and A. L. Taylor, *J. Appl. Phys.*, 1978, **49**, 1452.
13 K. Z. Rushchanskii, S. Kamba, V. Goian, P. Vanek, M. Savinov, J. Prokleska, D. Nuzhnyy, K. Knizek, F. Laufek, S. Eckel, S. K. Lamoreaux, A. O. Sushkov, M. Lezaic and N. A. Spaldin, *Nature materials*, 2010, **9**, 649–654.
14 K. Rubi, P. Kumar, D. M. Repaka, R. Chen, J.-S. Wang and R. Mahendiran, *Applied Physics Letters*, 2014, **104**, 32407.
15 T. Wei, Q. J. Zhou, X. Yang, Q. G. Song, Z. P. Li, X. L. Qi and J.-M. Liu, *Applied Surface Science*, 2012, **258**, 4601–4606.
16 H. Wu, Q. Jiang and W. Z. Shen, *Phys. Rev. B*, 2004, **69**.
17 G. J. Snyder and E. S. Toberer, *Nature materials*, 2008, **7**, 105–114.
18 Z. H. Dughaish, *Physica B: Condensed Matter*, 2002, **322**, 205–223.
19 P. Sun, B. Wei, J. Zhang, J. M. Tomczak, Am Strydom, M. Søndergaard, B. B. Iversen and F. Steglich, *Nature communications*, 2015, **6**.
20 B. G. Streetman and S. Banerjee, *Solid state electronic devices*, Prentice Hall New Jersey, 2000.
21 W. D. Callister and D. G. Rethwisch, *Materials science and engineering: an introduction*, Wiley New York, 2007.
22 A. Shkabko, C. Xu, P. Meuffels, F. Gunkel, R. Dittmann, A. Weidenkaff and R. Waser, *Apl Materials*, 2013, **1**, 52111.
23 M. Tsukioka, J. Tanaka, Y. Miyazawa, Y. Mori, H. Kojima and S. Ehara, *Solid State Communications*, 1979, **32**, 223–227.
24 L. Sagarna, K. Z. Rushchanskii, A. Maegli, S. Yoon, S. Populoh, A. Shkabko, S. Pokrant, M. Ležaić, R. Waser and A. Weidenkaff, *Journal of Applied Physics*, 2013, **114**, 33701.
25 J. O. Sofo and G. D. Mahan, *Physical Review B*, 1994, **49**, 4565.
26 R. Ang, A. U. Khan, N. Tsujii, K. Takai, R. Nakamura and T. Mori, *Angewandte Chemie International Edition*, 2015, **54**, 12909–12913.
27 N. Tsujii and T. Mori, *Applied Physics Express*, 2013, **6**, 43001.
28 S. Saha, T. P. Sinha and A. Mookerjee, *Physical Review B*, 2000, **62**, 8828.
29 S. R. Gilbert, L. A. Wills, B. W. Wessels, J. L. Schindler, J. A. Thomas and C. R. Kannewurf, *Journal of Applied Physics*, 1996, **80**, 969–977.

30 T. Birol and C. J. Fennie, *Physical Review B*, 2013, **88**, 94103.
31 R. t. Shannon, *Acta Crystallographica Section A: Crystal Physics, Diffraction, Theoretical and General Crystallography*, 1976, **32**, 751–767.
32 H. M. Rietveld, *Acta Crystallographica*, 1967, **22**, 151–152.
33 H. Rietveld, *Journal of applied Crystallography*, 1969, **2**, 65–71.
34 J. Rodriguez-Carvajal, *FullProf. 2k, version 5.30, March 2012*, ILL.
35 A. P. Hammersley, S. O. Svensson, M. Hanfland, A. N. Fitch and D. Hausermann, *International Journal of High Pressure Research*, 1996, **14**, 235–248.
36 G. Ashiotis, A. Deschildre, Z. Nawaz, J. P. Wright, D. Karkoulis, F. E. Picca and J. Kieffer, *Journal of applied Crystallography*, 2015, **48**, 510–519.
37 A. C. Larson and R. B. von Dreele, *General Structure Analysis System. LANSCE, MS-H805, Los Alamos, New Mexico*, 1994.
38 T. Egami and S. J. L. Billinge, *Underneath the Bragg peaks: structural analysis of complex materials*, Elsevier, 2003.
39 P. Juhás, T. Davis, C. L. Farrow and S. J. L. Billinge, *Journal of applied Crystallography*, 2013, **46**, 560–566.
40 C. L. Farrow, P. Juhas, J. W. Liu, D. Bryndin, E. S. Božin, J. Bloch, T. Proffen and S. J. Billinge, *Journal of Physics: Condensed Matter*, 2007, **19**, 335219.
41 G. Kresse and D. Joubert, *Physical Review B*, 1999, **59**, 1758.
42 J. Heyd, G. E. Scuseria and M. Ernzerhof, *The Journal of Chemical Physics*, 2003, **118**, 8207–8215.
43 M. Scavini, M. Coduri, M. Allieta, M. Brunelli and C. Ferrero, *Chemistry of Materials*, 2012, **24**, 1338–1345.
44 M. Scavini, M. Coduri, M. Allieta, P. Masala, S. Cappelli, C. Oliva, M. Brunelli, F. Orsini and C. Ferrero, *IUCrJ*, 2015, **2**, 511–522.
45 M. S. Senn, D. A. Keen, T. C. Lucas, J. A. Hriljac and A. L. Goodwin, *Physical review letters*, 2016, **116**, 207602.
46 M. Allieta, M. Scavini, L. J. Spalek, V. Scagnoli, H. C. Walker, C. Panagopoulos, S. S. Saxena, T. Katsufuji and C. Mazzoli, *Physical Review B*, 2012, **85**, 184107.
47 S. Y. Chong, R. J. Szczecinski, C. A. Bridges, M. G. Tucker, J. B. Claridge and M. J. Rosseinsky, *Journal of the American Chemical Society*, 2012, **134**, 5836–5849.
48 K. Datta, A. Richter, M. Göbbels, D. A. Keen and R. B. Neder, *Physical Review B*, 2016, **93**, 64102.

49 G. H. Kwei, A. C. Lawson, S. J. Billinge and S. W. Cheong, *The Journal of Physical Chemistry*, 1993, **97**, 2368–2377.
50 W. H. Baur, *Acta Crystallographica Section B: Structural Crystallography and Crystal Chemistry*, 1974, **30**, 1195–1215.
51 A. V. Kovalevsky, S. Populoh, S. G. Patrício, P. Thiel, M. C. Ferro, D. P. Fagg, Frade, JR and A. Weidenkaff, *The Journal of Physical Chemistry C*, 2015, **119**, 4466–4478.
52 L. Zhang, T. Tosho, N. Okinaka and T. Akiyama, *MATERIALS TRANSACTIONS*, 2008, **49**, 2868–2874.
53 L. Sagarna, A. Shkabko, S. Populoh, L. Karvonen and A. Weidenkaff, *Applied Physics Letters*, 2012, **101**, 33908.
54 M. Yamamoto, H. Ohta and K. Koumoto, *Applied Physics Letters*, 2007, **90**, 072101-1.
55 R. R. Heikes and R. W. Ure, *Thermoelectricity: science and engineering*, Interscience Publishers, 1961.
56 R. Ranjan, H. S. Nabi and R. Pentcheva, *Journal of Physics: Condensed Matter*, 2007, **19**, 406217.
57 W. Koshibae and S. Maekawa, *Physical review letters*, 2001, **87**, 236603.
58 J. Kuneš and W. E. Pickett, *Physical Review B*, 2004, **69**, 165111.
59 P. M. Chaikin and G. Beni, *Physical Review B*, 1976, **13**, 647.
60 H. W. Eng, P. W. Barnes, B. M. Auer and P. M. Woodward, *Journal of Solid State Chemistry*, 2003, **175**, 94–109.
61 G. V. Lewis and C. R. Catlow, *Journal of Physics and Chemistry of Solids*, 1986, **47**, 89–97.
62 M. Miyauchi, M. Takashio and H. Tobimatsu, *Langmuir*, 2004, **20**, 232–236.
63 M. Cardona, *Physical Review*, 1965, **140**, A651.
64 J. H. Lee, X. Ke, N. J. Podraza, L. F. Kourkoutis, T. Heeg, M. Roeckerath, J. W. Freeland, C. J. Fennie, J. Schubert and D. A. Muller, *Applied Physics Letters*, 2009, **94**, 212509.
65 L. Sagarna, S. Populoh, A. Shkabko, J. Eilertsen, A. E. Maegli, R. Hauert, M. Schrade, L. Karvonen and A. Weidenkaff, *The Journal of Physical Chemistry C*, 2014, **118**, 7821–7831.
66 N. F. Mott and E. A. Davis, *Electronic processes in non-crystalline materials*, OUP Oxford, 2012.

67 Y. Wang, Y. Sui, X. Wang and W. Su, *Journal of Physics D: Applied Physics*, 2009, **42**, 55010.
68 H. Ihrig, *Journal of Physics C: Solid State Physics*, 1976, **9**, 3469.
69 N. Wang, H. Chen, H. He, W. Norimatsu, M. Kusunoki and K. Koumoto, *Scientific reports*, 2013, **3**.
70 H. Muta, A. Ieda, K. Kurosaki and S. Yamanaka, *MATERIALS TRANSACTIONS*, 2005, **46**, 1466–1469.
71 H. Muta, K. Kurosaki and S. Yamanaka, *Journal of Alloys and Compounds*, 2004, **368**, 22–24.
72 W. G. Zeier, A. Zevalkink, Z. M. Gibbs, G. Hautier, M. G. Kanatzidis and G. J. Snyder, *Angewandte Chemie International Edition*, 2016, **55**, 6826–6841.
73 A. V. Kovalevsky, A. A. Yaremchenko, S. Populoh, P. Thiel, D. P. Fagg, A. Weidenkaff and Frade, JR, *Physical Chemistry Chemical Physics*, 2014, **16**, 26946–26954.
74 Z. Lu, H. Zhang, W. Lei, D. C. Sinclair and I. M. Reaney, *Chemistry of Materials*, 2016, **28**, 925–935.
75 A. A. Yaremchenko, S. Populoh, S. G. Patrício, J. Macías, P. Thiel, D. P. Fagg, A. Weidenkaff, J. R. Frade and A. V. Kovalevsky, *Chemistry of Materials*, 2015, **27**, 4995–5006.

Graphical TOC

Tailoring the structure and thermoelectric properties of $BaTiO_3$ via Eu^{2+} substitution